

Single Ion Implantation Into Si-Based Devices

B. C. Johnson^a, G. C. Tettamanzi^b, C. Yang^a, A. D. C. Alves^a, J. van Donkelaar^a, S. Thompson^a, J. Verduijn^b, J. A. Mol^b, R. Wacquez^c, M. Vinet^d, A. S. Dzurak^e, M. Sanquer^c, S. Rogge^b and D. N. Jamieson^a

^a Centre of Excellence for Quantum Computer Technology, School of Physics, University of Melbourne, Victoria 3010, Australia

^b Kavli Institute of Nanoscience, Delft University of Technology, Lorentzweg 1, 2628 CJ Delft, The Netherlands,

^c INAC-SPSMS, CEA-Grenoble, 17 rue des martyrs, F-38054 Grenoble, France

^d LETI-Minatec, CEA-Grenoble, 17 rue des martyrs, F-38054 Grenoble, France

^e Centre of Excellence for Quantum Computer Technology, School of Electrical Engineering and Telecommunications, University of New South Wales, Sydney NSW 2052, Australia.

Deterministic doping is crucial for overcoming dopant number variability in present nano-scale devices and for exploiting single atom degrees of freedom. The development of deterministic doping schemes is required. Here, two approaches to the detection of single ion impact events in Si-based devices are reviewed. The first is via specialized PiN structures where ions are directed onto a target area around which a field effect transistor can be formed. The second approach involves monitoring the drain current modulation during ion irradiation. We investigate the detection of both high energy He⁺ and 14 keV P⁺ dopants. The stopping of these ions is dominated by ionization and nuclear collisions, respectively. The optimization of the implant energy for a particular device and post-implantation processing are also briefly considered.

Introduction

Random variations in the number and placement of dopants in classical metal-oxide-semiconductor field-effect-transistors (MOSFETs) are already major issues for CMOS devices operating at room temperature.[1] At 4 K quantum mechanical dependent functionalities have been observed in ultra-scaled MOSFETs with single adventitiously placed dopants.[2-4] In these devices the Bohr radius of a dopant atom is a significant fraction of the device size. Deterministic doping technologies aim to mitigate random variations in the doping while also allowing for the controlled fabrication of these ultra-scaled devices. In addition, deterministic doping provides significant potential for solid-state quantum computers.[5-8] For example, the spin-dependent transport between a single ³¹P atom and a single electron transistor has been proposed as a sensitive way to detect and control the P atom spin state.[9] Such an architecture requires the precise placement of a single P donor above which a shorted coplanar transmission line is deposited. This transmission line both carries microwave pulses that produce an oscillating magnetic field for local electron spin resonance and a dc bias as recently demonstrated.[10]

Single ion implantation and detection has been reported by a number of groups.[11-19] These works are compared in Table I. The table shows the energy and type of implanted ion as well as the target type and detection scheme used. Low energy single dopant implantation into both micron-scale and nano-scale devices has been reported (indicated by the bold text in Table I).[11,15,19] Deterministic P implantation was achieved by the detection of the electron-hole (e-h) pairs created by the ion impact with an integrated PiN structure.[11] This scheme has resulted in a device where the time-resolved control and transfer of a single electron between two deterministically implanted P atoms was observed.[20] Other detection schemes are based on ion impact signals from secondary electrons[14,16,18] or the modulation of the drain current, I_d . [13,15,17,19] For I_d modulation, discrete downward steps in I_d have been observed with low energy Si^{2+} implantation into a micron-scale SOI channel.[17] However, for micron-scale MOSFETs, other reports show discrete upward steps.[13,15]

TABLE I. Review of single ion implantation technology in the keV regime to date. Donors are in bold text.

Ion	Energy (keV)	Device (size)	Detection method	References	Stopping (ionization/recoils) ^a
$^{31}\text{P}^+$	14	PiN junction ($100 \mu\text{m}^2$)	e-h pair generation	[11]	42/6
$^2\text{H}^+$	250	Avalanche diode (μm^2)	e-h pair generation	[12]	99/1
$^{121}\text{Xe}^{6+}$	48	MOSFET ($4 \mu\text{m}^2$)	I_d modulation	[13]	41/5
$^{40}\text{Ar}^{2+}$	6	-	Secondary electrons	[14]	35/6
$^{131}\text{Xe}^{30+}$	195	-	Secondary electrons	[14]	50/5
$^{209}\text{Bi}^{45+}$	120	-	Secondary electrons	[14]	47/5
$^{121}\text{Sb}^{14+}$	70	MOSFET ($4 \mu\text{m}^2$)	I_d modulation	[15]	41/6
$^{121}\text{Sb}^{12+}$	60	MOSFET ($4 \mu\text{m}^2$)	I_d modulation	[15]	41/6
$^{131}\text{Xe}^{6+}$	50	MOSFET ($4 \mu\text{m}^2$)	I_d modulation	[15]	41/6
$^{31}\text{P}^{13+}$	39	-	Secondary electrons	[16]	51/5
$^{126}\text{Te}^{33+}$	99	-	Secondary electrons	[16]	44/6
$^{28}\text{Si}^{2+}$	30	SOI channel ($0.96 \mu\text{m}^2$)	I_d modulation	[17]	50/5
$^{31}\text{P}^+$	30	SOI channel ($0.96 \mu\text{m}^2$)	Secondary electrons	[18]	42/6
$^4\text{He}^+$	500	MOSFET($1500\text{-}2700 \text{ nm}^2$)	I_d modulation	[19]	98/1
$^{31}\text{P}^+$	14	MOSFET($1500\text{-}2700 \text{ nm}^2$)	I_d modulation	[19]	42/6

^a These values represent the percentage of the total energy lost to ionization and nuclear recoils, respectively as calculated with SRIM. Additional energy loss occurs via phonon generation.

In this paper we review two methods for single ion implantation. These are e-h pair detection with integrated PiN structures and I_d modulation in nano-scale SOI MOSFETs. The behavior of these devices under high-energy He^+ and 14 keV P^+ irradiation is discussed. The dominant mechanism for the dissipation of kinetic energy of He^+ ions and P^+ dopants is electronic stopping and nuclear stopping, respectively. The percentage of the total implanted ion energy lost to ionization (electronic stopping) and nuclear recoils (nuclear stopping) as calculated by the Monte Carlo code SRIM[22] is shown in the last column of Table I. The dominant stopping process determines the signal to noise ratio in

the integrated PiN structures and the step direction in the I_d modulation scheme. The next section discusses these stopping processes further as well as the optimization of the implant energy and post-implantation processing for device fabrication. Single ion detection with the integrated PiN diodes and I_d modulation is then discussed in the proceeding two sections followed by concluding remarks.

Background

The He and P implants used in these experiments result in quite different damage profiles as illustrated in Fig. 1 for 500 keV He^+ ions and 14 keV P^+ dopants. This figure shows the implantations into a SOI structure as calculated by SRIM. The energy of the implanted ion determines whether this energy is imparted to the target device via electronic or nuclear stopping processes. In the near surface region fast ions will ionize the target atoms via electronic stopping. As the energy decreases nuclear stopping begins to dominate energy loss resulting in atomic displacements and lattice damage. Fig. 1a) shows the concentration of vacancies as a function of depth after the implantation of $1 \times 10^{12} \text{ cm}^{-2}$ He^+ and P^+ . An order of magnitude more damage is caused by the P^+ implant than the He^+ implant in the channel of the SOI structure. Conversely, He^+ causes about twice as many ionizations than the implanted P^+ as shown in Fig. 1b). The number of ionizations created in the buried oxide (BOX) layer is much greater for the He^+ implant case. Assuming that an e-h pair is produced with every 18 eV of ionization, it is expected that a maximum of around 3900 e-h pairs are produced by a single He^+ in the BOX layer compared to just 6 by P^+ . Indeed, this illustrates that the mechanism by which implanted ions are detected may depend greatly on the type of implanted ion. For implantation into a SOI structure it is likely that the I_d modulation caused by P^+ is due to damage created in the channel region whereas He^+ causes ionizations in the BOX layer. Such ionizations

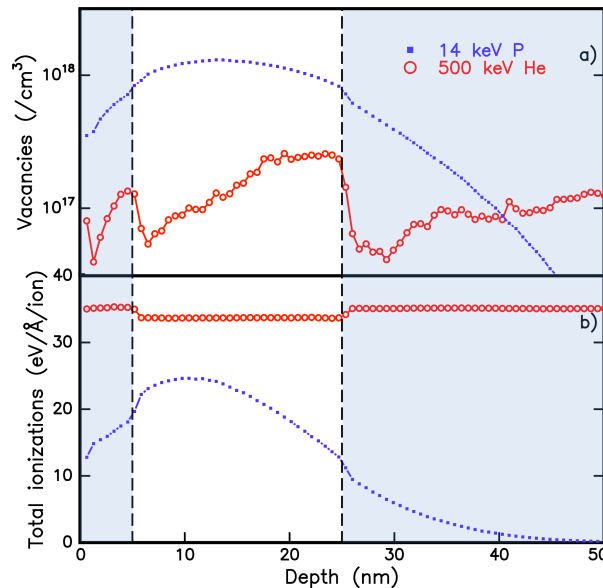


Figure 1: SRIM simulation of (a) the vacancy distribution created by 500 keV He^+ and 14 keV P^+ implanted into the SOI nano-MOSFET to a fluence of $1 \times 10^{12} \text{ cm}^{-2}$ and (b) the total ionizations per Ångstrom per ion. The vertical dashed lines indicate the Si/SiO₂ interfaces either side of the channel between the gate oxide and the BOX.

can result in trapped holes which can shift the threshold voltage.[23] Further, the He^+ implant will create a much stronger signal in detection schemes that depend on the generation of e-h pairs such as in the integrated PiN diodes.

While we demonstrate that a discrete number of ions can be implanted, they are subject to random statistical processes that cause straggle in the ion range. Figure 2 shows the probability of the implanted P^+ ion coming to rest in the channel of a SOI MOSFETs as a function of ion energy. The optimal energy is found to be 5.9 keV with a probability of 90%. In comparison, 14 keV P^+ results in a 57% chance of the P^+ stopping within the channel.

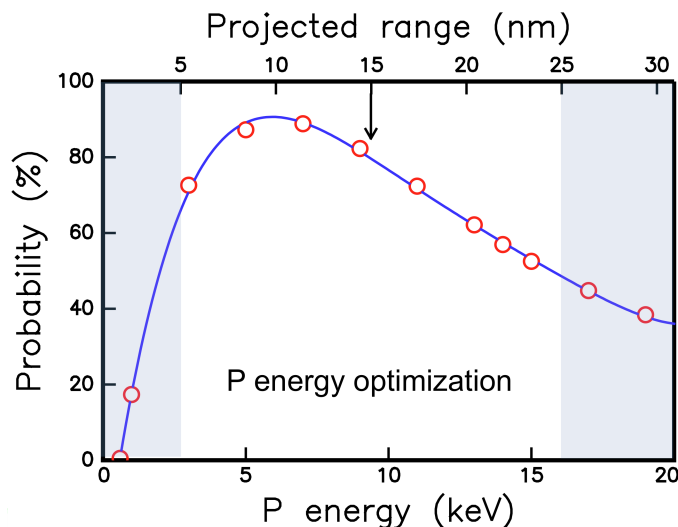


Figure 2: The probability of placing the P atom somewhere in the channel of the SOI nano-MOSFET device for dopant implant energy optimization. The shaded area represents the SiO_2 part of the SOI device.

The position of the implanted dopant is also subject to diffusion during post-implantation processing. Firstly, implantation must be performed through the gate oxide in order to avoid thermal diffusion during high temperature oxidization unless a dopant with a low diffusion coefficient is chosen such as Sb.[24-25] Alternatively, a low temperature high-quality oxide growth may be performed after implantation to avoid any significant dopant diffusion.[26] Here, we discuss devices where the implantation is performed through the oxide itself. Implantation through a 5 nm oxide layer followed by a rapid thermal anneal (RTA) has been shown not to increase the SiO_2/Si interface trap density and was in fact found to be beneficial when the as-grown oxide interface trap density is abnormally high.[27]

The 14 keV P^+ implant has also been simulated using the analytical profiles in FLOOPS ISE TCAD[28] and is shown in Fig. 3. Fig. 3a) shows the 2D depth profile of the 14 keV P^+ implanted to a fluence of $1 \times 10^{11} \text{ cm}^{-2}$ through a 5 nm wide surface mask. The lateral straggle is shown to be much less than the projected straggle as expected. Fig. 3b) and c) show the profile as a function of depth and in the lateral direction at a depth of 14.8 nm. There is a slight asymmetry in the lateral profile since an implant angle of 7° with a tilt of 10° was used in order to avoid channeling. The simulated profile after a 1000°C , 5s rapid thermal anneal is also shown. It can be seen that the dopant diffusion is

not significant when this dopant activation anneal is employed. The next section briefly reviews the use of integrated PiN diodes for the detection of single ions.

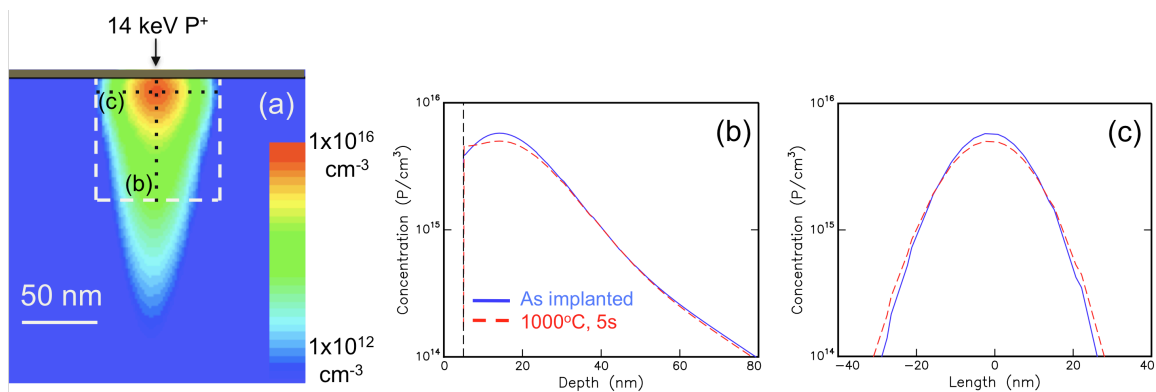


Figure 3. (a) 2D depth profile of a 14 keV P^+ implant into a Si substrate with a 5 nm oxide using FLOOPS. The dashed line represents a $80 \times 80 \text{ nm}^2$ boundary around the implanted region. The dotted lines labeled (b) and (c) (at a depth of 14.8 nm) indicate the line along which Figs. (b) and (c) are determined. In (b) and (c) the as-implanted (solid line) and 1000°C , 5 s annealed (dashed line) profiles are compared.

Integrated PiN structures

Figure 4 shows a schematic of the integrated PiN structure. It consists of two surface Al detector electrodes that make contact with two boron-doped wells in high resistivity silicon. There is a central implant zone between the two p-wells with a surface oxide 5 nm thick. The rest of the device is covered with a 200-300 nm thick field oxide. A back layer contact is formed by P in-diffusion. During operation the detector is cooled to liquid nitrogen temperature to reduce the leakage current. At 120 K the leakage is generally around $< 10 \text{ pA}$ for these devices. A voltage of 10-20 V is applied creating a depletion region throughout the substrate. The implanted ion is then directed through a surface mask or aperture. When the ion enters the substrate e-h pairs are created and a current is then detected.[11,29] The signal from a 14 keV P^+ ion is shown in Fig. 5. After implantation the device undergoes various post-implantation fabrication steps. This involves the formation of a MOSFET type structure around the central window.[20]

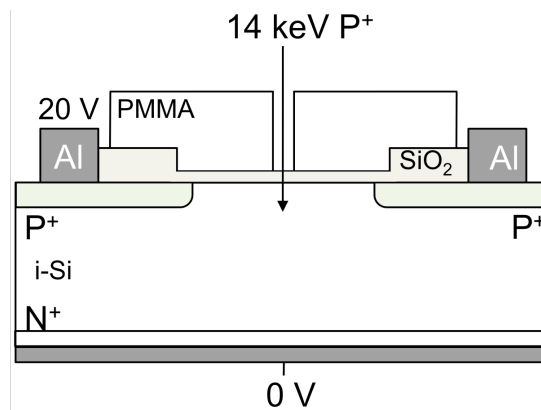


Figure 4. Schematic diagram of the PiN single ion detector integrated into a MOS structure.

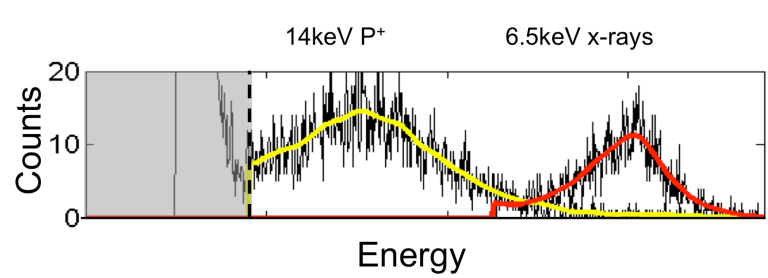


Figure 5. Energy spectrum of a single P^+ ion impact in the integrated PiN structure. The shaded region indicates the noise threshold. The pulse from a 6.5 keV x-ray in the same device is shown for comparison.

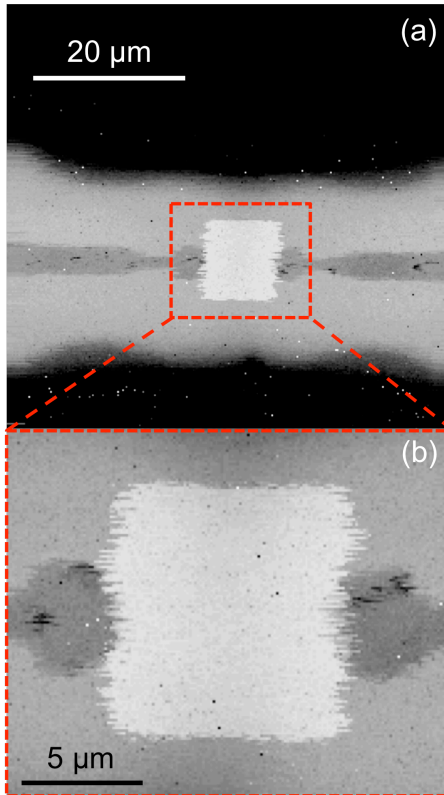


Figure 6. (a) IBIC map of the integrated PiN structure measured at room temperature. (b) Shows a close-up of the central target region in (a).

The PiN detector collection efficiency can be measured with the ion beam induced current (IBIC) technique. An IBIC map of the device is shown in Fig. 6 for a 2 MeV He^+ ion beam scanned across the device. The map was collected at room temperature where the detector is generally much noisier. However, detection is possible at this temperature because the number of ionizations created by the He^+ beam is much greater than the P^+ beam as shown in Fig. 1 above. The charge collection efficiency is close to 100% in the central implant region for pristine devices since the collection time is much less than the recombination time. In the I_d modulation detection scheme in SOI nano-FETs discussed in the next section both He^+ and P^+ ions can be detected at room temperature.[19] However, detection depends on the creation of either trapped oxide charge in the BOX or Frenkel pairs in the channel.

Nano-scale silicon on insulator FETs

The detection of single ions via I_d modulation is most appropriate when the current density is confined to a narrow channel as in a SOI nano-FET. Such devices are also promising architectures for the realization of new single-atom functionalities.[30] The dimensions of the SOI nano-FETs discussed here are listed in Table. II. Again, these devices have a gate oxide thickness of 5 nm [31] and the SiO₂/Si interface is expected to have an interface state density in the mid-10¹⁰ eV⁻¹.cm⁻² as measured by deep level transient spectroscopy. Two MOSFET types were considered and are shown schematically in Fig. 7. The first was a single gate MOSFET with full back-end processing that incorporated a surface passivation layer and was used for the He implantation experiments. The second type was a double gated MOSFET with a spacing between the two gates of $S_g=50$ nm. Si₃N₄ was formed around each gate leaving a space through which the channel was exposed to the ion beam.[3]

TABLE II. Summary of the devices under study.

ID	Gate type	L xW x H (nm ²)	Estimated fluence (cm ⁻²)	Total exposure ^a	Counted ions	V _g (V)
P1	Double	25 x 70 x 20 ^b	5x10 ¹²	6x10 ¹ P	2	0.6
He1	Single	25 x 60 x 20	3x10 ¹²	5x10 ¹ He	-	grounded
He2	Single	45 x 60 x 20	3x10 ¹²	8x10 ¹ He	30	0.8

^aUpper limit of implanted ions into the device subject to Poisson statistics and experimental uncertainties.

^bThe exposed space between the two gates on top of the channel, S_g , was 50 nm wide. Si₃N₄ spacers decrease the exposed area further.

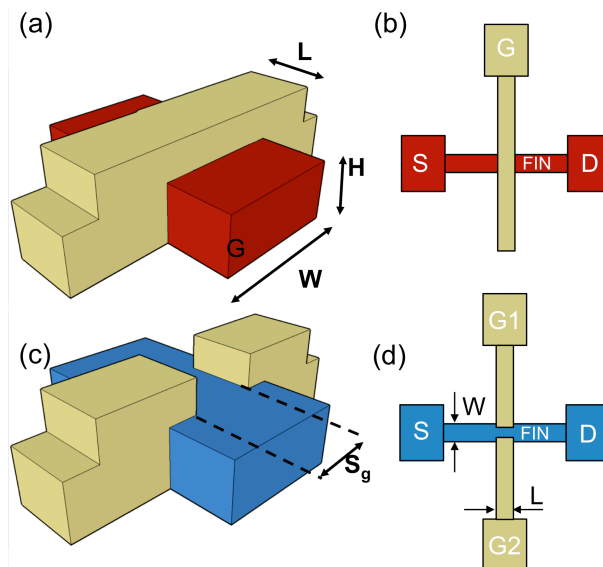


Figure 7: Schematics of the devices with channel width (W), length (L) and height (H) are shown. S_g is the spacing between the gates on top of the channel.

Figure 8 shows the I_d characteristics before, during and after implantation. Fig. 8a) shows the I_d modulation while the He⁺ beam was scanned across the device with a beam flux of $\sim 7 \times 10^{12}$ ions/cm²/s. The device (He2 in Table II) was biased to 0.8 V during implantation. Fig. 8b) shows the I_d modulation during P⁺ irradiation into device P1 with a P⁺ beam directed through a stationary 600 μ m diameter aperture at an average flux of $\sim 2 \times 10^9$ ions/cm²/s. Discrete steps in I_d are observed in both cases and represented by peaks in the dI_d/dt plots shown in the lower panel of Figs. 8a) and b). For P1 I_d

modulation two discrete steps in I_d are observed. The second step is shown in the inset on a different scale. The time constant of this second step is much larger than the first and its height is also much smaller, most likely as a consequence of the transformation of a significant volume of the channel as a result of the first P^+ impact. This limits the number of dopants that can be implanted before an anneal is required. After irradiation, the devices remain robust and no observable change in gate leakage current is observed.

Figures 8c) and d) show the IV curves for devices He1, He2 and P1 before and one day after the implants. The He^+ and P^+ implantation-induced defects modify the IV curves in different ways. The positive trapped oxide charge created in the BOX by the He implants can result in an inversion layer formed along the Si/BOX interface which causes interface coupling effects.[32-34] This results in the observed negative shift. The charge density was estimated using analytical expressions of the sub-threshold I_d at mid-gap to be $5.0 \times 10^{12} \text{ cm}^{-2}$ for both He1 and He2.[35] In addition to a shift, there is a noticeable stretch-out, the extent of which is indicated by the sub-threshold swing, S , in Fig. 8c) and d). We find the associated change in interface trap density is $4.3 \times 10^{12} \text{ cm}^{-2} \text{ eV}^{-1}$ and $5.5 \times 10^{12} \text{ cm}^{-2} \text{ eV}^{-1}$ for devices He1 and He2, respectively. These values are only approximate since the analytical expressions assume a lateral device and a homogenous defect distribution. The latter may not be appropriate when considering single ion impact events. For device He2 there is variation in the I_d modulation step height. It is expected that this is due to the threshold voltage shift being most sensitive where the current density is high. After the beam was no longer incident on He2, I_d began to decrease over a longer time scale. This is indicative of the recombination of positive trapped oxide charge [36] and was not observed for P^+ implanted devices.

The P^+ implantation caused quite different behavior as seen in Fig. 8d). A positive shift is observed suggesting that the interface states are negatively charged as is the case for n-type MOSFETs.[37] This shift corresponds to a charge density of $1.5 \times 10^{12} \text{ cm}^{-2}$. A general decrease in I_d is also observed suggesting an increase in series resistance consistent with the introduction of Frenkel pairs in the channel.

Conclusion

The implantation of single ions via two methods was reviewed. Integrated PiN structures are used to detect single ion impacts via the creation of e-h pairs. IBIC was used to map the charge collection efficiency with the greatest efficiency found in the target region through which P^+ can be directed into the substrate. In the I_d modulation scheme ionizations in the BOX created by He^+ implantation caused I_d to step upward. In contrast, Frenkel pairs created in the channel region by P^+ implantation caused downward steps. Both detection schemes are relatively sensitive ion impacts that result in a large number of ionizations. The optimization of the implant parameters and post-implantation processing also requires careful consideration.

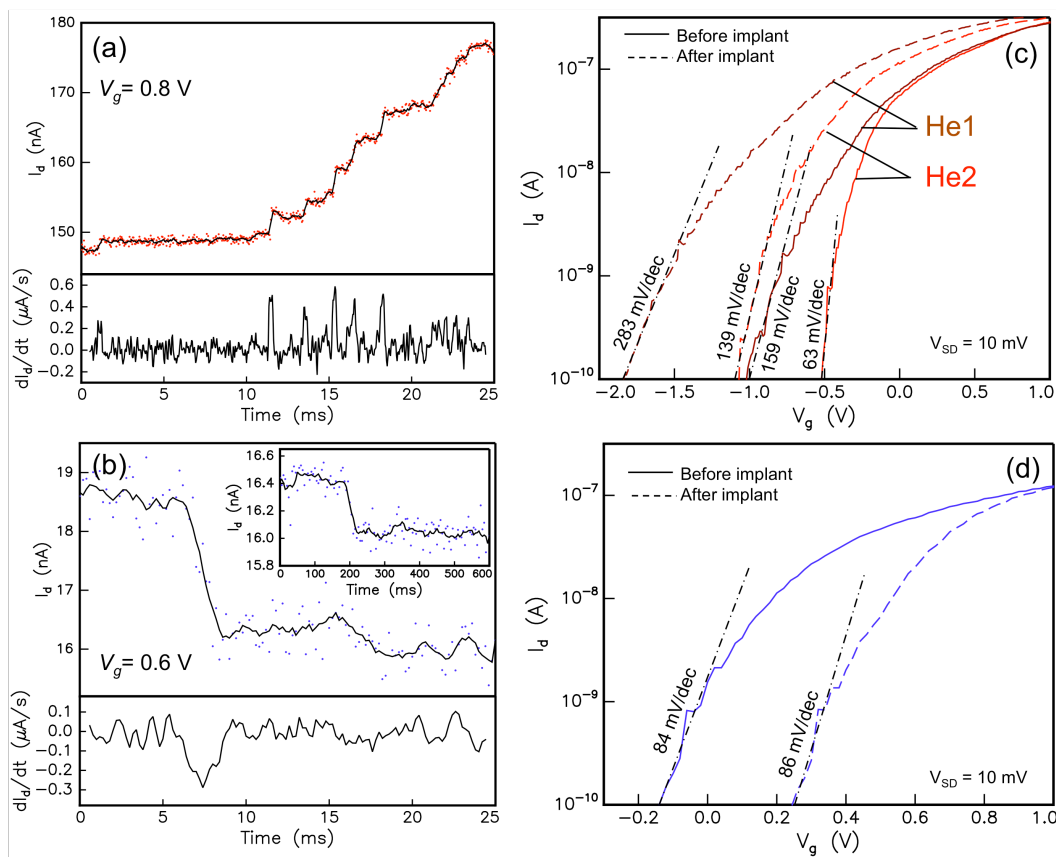


Figure 8. Nano-scale MOSFET I_d collected at a 100 kHz sample rate during (a) 500 keV He and (b) 14 keV P irradiation. Discrete steps represent single ion impacts. The time trace has been binned down to (a) 25 kHz, (b) 5 kHz and (inset of b) 0.2 kHz using the time scale of the step as a guide. The derivative is shown under each trace. The IV before and one day after irradiation are shown for devices (c) He1 and He2 and (d) P1.

Acknowledgments

Work on the integrated PiN structures is funded by the Australian Research Council Centre of Excellence Scheme and US Army Research Office under Contract No. W911NF-08-1-0527. The nano-MOSFET work is funded by the EC FP7 FET-proactive NanoICT projects MOLOC (215750) and AFSiD (214989) and the Dutch Fundamenteel Onderzoek der Materie FOM. The Education Infrastructure/Superscience Heavy Ion Accelerator Fund is acknowledged for supporting the University of Melbourne Pelletron laboratory.

References

1. "International technology roadmap for semiconductors", <http://www.itrs.net/> (2007)
2. G. Lansbergen, R. Rahman, C. J. Wellard, I. Woo, J. Caro, N. Collaert, S. Biesemans, G. Klimeck, L. C. L. Hollenberg, and S. Rogge, *Nat. Phys.* **41**, 656 (2008)

3. M. Pierre, R. Wacquez, X. Jehl, M. Sanquer, M. Vinet, and O. Cueto, *Nat. Nanotechnol.* **5**, 133 (2010)
4. M. Klein, J. A. Mol, J. Verduijn, G. P. Lansbergen, S. Rogge, R. D. Levine, and F. Remacle, *Appl. Phys. Lett.* **96**, 043107 (2010)
5. B. E. Kane, *Nature* **393**, 133 (1998)
6. R. Vrijen, E. Yablonovitch, K. Wang, H. W. Jiang, A. Balandin, V. Roychowdhury, T. Mor, and D. DiVincenzo, *Phys. Rev. A* **62**, 012306 (2000)
7. M. Friesen, P. Rugheimer, D. E. Savage, M. G. Lagally, D. W. van der Weide, R. Joynt, and M. A. Eriksson, *Phys. Rev. B* **67**, 121301 (2003)
8. L. C. L. Hollenberg, A. D. Greentree, A. G. Fowler, and C. J. Wellard, *Phys. Rev. B* **74**, 045311 (2006).
9. A. Morello, C. C. Escott, H. Huebl, L. H. Willems van Beveren, L. C. L. Hollenberg, D. N. Jamieson, A. S. Dzurak and R. G. Clark, *Phys. Rev. B* **80**, 081307 (2009).
10. L. H. Willems van Beveren, H. Huebl, D. R. McCamey, T. Duty, A. J. Ferguson, R. G. Clark and M. S. Brandt, *Appl. Phys. Lett.* **93**, 072102 (2008).
11. D. N. Jamieson, C. Yang, T. Hopf, S. M. Hearne, C. I. Pakes, S. Prawer, M. Mitic, E. Gauja, S. E. Andresen, F. E. Hudson, A. S. Dzurak, and R. G. Clark, *Appl. Phys. Lett.* **86**, 202101 (2005).
12. J. A. Seamons, E. Bielejec, M. S. Carroll, and K. D. Childs, *Appl. Phys. Lett.* **93**, 043124 (2008).
13. C. D. Weis, A. Schuh, A. Batra, A. Persaud, I. W. Rangelow, J. Bokor, C. C. Lo, S. Cabrini, E. Sideras-Haddad, G. D. Fuchs, R. Hanson, D. D. Awschalom, and T. Schenkel, *J. Vac. Sci. Technol. B* **26**, 2596 (2008).
14. A. Persaud, J. A. Liddle, T. Schenkel, J. Bokor, T. Ivanov, and I. W. Rangelow, *J. Vac. Sci. Technol. B* **23**, 2798 (2005).
15. A. Batra, C. D. Weis, J. Reijonen, A. Persaud, T. Schenkel, S. Cabrini, C. C. Lo, and J. Bokor, *Appl. Phys. Lett.* **91**, 193502 (2007).
16. A. Persaud, S. J. Park, J. A. Liddle, I. W. Rangelow, J. Bokor, R. Keller, F. I. Allen, D. H. Schneider, and T. Schenkel, *Quantum Inf. Process.* **3**, 233 (2004).
17. T. Shinada, T. Kurosawa, H. Nakayama, Y. Zhu, M. Hori, and I. Ohdomari, *Nanotechnology* **19**, 345202 (2008).
18. T. Shinada, S. Okamoto, T. Kobayashi and I. Ohdomari, *Nature* **437** 1128 (2005).
19. B. C. Johnson, G. C. Tettamanzi, A. D. C. Alves, S. Thompson, C. Yang, J. Verduijn, J. A. Mol, R. Wacquez, M. Vinet, M. Sanquer, S. Rogge and D. N. Jamieson, *Appl. Phys. Lett.* **96**, 264102 (2010).
20. S. E. S. Andresen, R. Brenner, C. J. Wellard, C. Yang, T. Hopf, C. C. Escott, R. G. Clark, A. S. Dzurak, D. N. Jamieson, and L. C. L. Hollenberg, *Nano Letters* **7**, 2000 (2007).
21. D. N. Jamieson, *Nucl. Inst. Meth. B* **130**, 706 (1997).
22. J. F. Ziegler, J. P. Biersack, and U. Littmark, “*The stopping and range of ions in solids (SRIM)*”, (1996), <http://www.srim.org/>
23. R. F. DeKeersmaecker and D. J. DiMaria, *J. Appl. Phys.* **51**, 532 (1980).
24. C. C. Lo, J. Bokor, T. Schenkel, J. He, A. M. Tyryshkin and S. A. Lyon, *Appl. Phys. Lett.* **91** 242106 (2007).
25. T. Schenkel, J. A. Liddle, A. Persaud, A. M. Tyryshkin, S. A. Lyon, R. deSousa, K. B. Whaley, J. Bokor, J. Shangkuan, and I. Chakarov, *Appl. Phys. Lett.* **88** 112101 (2006).
26. J.-Y. Zhang, I. W. Boyd, *Appl. Phys. Lett.* **71** 2964 (1997).

27. J. C. McCallum, M. L. Dunn, and E. Gauja, *Mater. Res. Soc. Symp. Proc.* **1074**, I12 (2008).
28. FLOOPS-ISE from ISE Integrated Systems Engineering, AG, Switzerland.
29. C. Yang, D. N. Jamieson, S. M. Hearne, C. I. Pakes, B. Rout, E. Gauja, A.J. Dzurak and R.G. Clark, *Nucl. Inst. Meth. B*, **190**, 212 (2002).
30. G. C. Tettamanzi, A. Paul, G. P. Lansbergen, J. Verduijn, S. Lee, N. Collaert, S. Biesemans, G. Klimeck, and S. Rogge, *IEEE Electron Device Letters* **31**, 150 (2010).
31. M. Pierre, R. Wacquez, B. Roche, X. Jehl, M. Sanquer, M. Vinet, E. Prati, M. Belli, and M. Fanciulli, *Appl. Phys. Lett.* **95**, 242107 (2009).
32. S. Cristoloveanu and V. Ferlet-Cavrois, “*Radiation effects and soft errors in integrated circuits and electronic devices*,” (World Scientific, 2004) p. 181
33. S. Eminente, S. Cristoloveanu, R. Clerc, A. Ohata, and G. Ghibaudo, *Solid State Electron.* **51**, 239 (2007).
34. F. Daugé, J. Pretet, S. Cristoloveanu, A. Vandooren, L. Mathew, J. Jomaah, and B. Y. Nguyen, *Solid State Electron.* **48**, 535 (2004).
35. P. J. McWhorter and P. S. Winokur, *Appl. Phys. Lett.* **48**, 133 (1986)
36. L. P. Trombetta, F. J. Feigl, and R. J. Zeto, *J. Appl. Phys.* **69**, 2512 (1991).
37. J. Srour and J. McGarrity, *Proceedings of the IEEE* **76**, 1443 (1988).